Nature of quasiparticle interference in three dimensions

Luke C. Rhodes,* Weronika Osmolska, Carolina A. Marques, and Peter Wahl
SUPA, School of Physics and Astronomy, University of St Andrews, North Haugh, St Andrews, Fife KY16 9SS, United Kingdom

(Received 1 August 2022; revised 22 November 2022; accepted 28 November 2022; published 5 January 2023)

Quasiparticle interference (QPI) imaging is a powerful tool for the study of the low-energy electronic structure of quantum materials. However, the measurement of QPI by scanning tunneling microscopy (STM) is restricted to surfaces and is thus inherently constrained to two dimensions. QPI has proved immensely successful for the study of materials that exhibit a quasi-two-dimensional electronic structure, yet it raises questions about how to interpret QPI in materials that have a highly three-dimensional electronic structure. In this paper, we address this question and establish the methodology required to simulate and understand QPI arising from three-dimensional systems as measured by STM. We calculate the continuum surface Green's function in the presence of a defect, which captures the role of the surface and the vacuum decay of the wave functions. We find that defects at different depths from the surface will produce unique sets of scattering vectors for three-dimensional systems, which nevertheless can be related to the three-dimensional electronic structure of the bulk material. We illustrate the consequences that the three-dimensionality of the electronic structure has on the measured QPI for a simple cubic nearest-neighbor tight-binding model, and then demonstrate application to a real material using a realistic model for PbS. Our method unlocks the use of QPI imaging for the study of quantum materials with three-dimensional electronic structures and introduces a framework to generically account for k_z dispersions within QPI simulations.

DOI: 10.1103/PhysRevB.107.045107

I. INTRODUCTION

Quasiparticle interference (QPI), the spatial perturbation to the local density of states (LDOS) in the presence of defects or boundaries, is an important phenomenon that enables scanning tunneling microscopy (STM), a real-space technique, to uncover information about electronic states in momentum space [1,2] with unparalleled energy resolution [3]. The perturbations due to QPI arise as a direct result of scattering between two electronic states and therefore measuring the Fourier transform of these spatial perturbations provides a route to uncover the electronic structure of a material [4,5].

These measurements have been immensely successful in understanding materials with a highly two-dimensional (2D) electronic structure, such as the cuprates [6–8] and ruthenates [9,10], where a comparison between experimental measurements and theoretical models is rather straightforward. On the other hand, in anisotropic materials with non-negligible interlayer hopping, such as the iron-based superconductors [11–13] or heavy-fermion systems [14–16], it has become apparent that the resulting three-dimensionality of the electronic structure results in visible changes to the measured QPI beyond a simple 2D model [17,18].

The challenge to understand the QPI of 3D electronic structures is fundamentally linked to the fact that STM is a surface-sensitive technique, limited to measuring the LDOS at surfaces and in two spatial dimensions. This raises an important question about how to interpret Fourier transforms of QPI measurements in systems that have a notable three-dimensional electronic structure.

Previous theoretical and experimental work studying the QPI of 3D electronic structures have shown that the direction and intensity of the QPI standing wave patterns are controlled by the Fermi velocity of the electronic states [19–21]. More recently, in conjunction with the experimental constraint that STM is a local technique, it has been argued that any standing waves generated by electronic states which have finite group velocity in the z direction [20], will actually traverse into the bulk of the material and therefore not generate a coherent long-range QPI signal that would be noticeable as sharp peaks in the Fourier transform [18,22].

So far, however, these arguments have not considered the role that the surface has on the electronic states, where k_z is no longer a good quantum number. In this paper, we address this issue by theoretically studying the consequence that the surface has on the formation of QPI. By utilizing the recently developed continuum LDOS (cLDOS) technique [23,24], which takes into account the inter-unit-cell superposition of the electronic states above the surface of a material, we show that information about the bulk 3D electronic structure can be readily obtained from experimental QPI measurements. We additionally show that defects at different distances from the surface will produce unique QPI patterns and that a full comparison between theory and experiment requires the consideration of defects at both different sites and depths from the surface.

II. THEORETICAL FRAMEWORK

To simulate Fourier-transformed QPI, we begin by calculating the cLDOS $\rho(\mathbf{r}, \omega)$ using the continuum Green's function $G(\mathbf{r}, \mathbf{r}, \omega)$ following Refs. [10,23,24],

$$\rho(\mathbf{r}, \omega) = -\frac{1}{\pi}\mathrm{Im}\, G(\mathbf{r}, \mathbf{r}, \omega). \quad (1)$$

*Corresponding author: lcr23@st-andrews.ac.uk

Here, $\mathbf{r}$ is a 3D continuous real-space vector, ω is the energy, and the continuum Green's function is defined via the continuum transformation of the discrete lattice Green's function, $G(\mathbf{R}, \mathbf{R}', \omega)$, in the presence of a pointlike impurity,

$$G(\mathbf{r}, \mathbf{r}', \omega) = \sum_{R} \sum_{R'} G(\mathbf{R}, \mathbf{R}', \omega) W(\mathbf{R} - \mathbf{r}) W(\mathbf{R}' - \mathbf{r}'). \tag{2}$$

Here, $\mathbf{R}$ is the discrete lattice vector and $W(\mathbf{R} - \mathbf{r})$ is a localized Wannier function connecting the discrete and continuous space.

The discrete lattice Green's function in the presence of a defect is obtained from the unperturbed lattice Green's function ($G^0(\mathbf{R}, \omega)$) using the T-matrix formalism,

$$G(\mathbf{R}, \mathbf{R}', \omega) = G^0(\mathbf{R} - \mathbf{R}', \omega) + G^0(\mathbf{R}, \omega) T(\omega) G^0(-\mathbf{R}', \omega) \tag{3}$$

where $T(\omega)$ describes the scattering from a single pointlike defect,

$$T(\omega) = \hat{V}[\hat{1} - \hat{V} G^0(\mathbf{R} = \mathbf{0}, \omega)]^{-1}. \tag{4}$$

Here, we use $\hat{V} = 100$ meV and $G^0(\mathbf{R}, \omega)$ is the Fourier transform of the noninteracting Green's function $G^0(\mathbf{k}, \omega)$ obtained from

$$G^0(\mathbf{k}, \omega) = [(\omega + i\Gamma)\hat{1} - H(\mathbf{k})]^{-1}. \tag{5}$$

We calculate $G^0(\mathbf{R}, \omega)$ via a Fourier transform of $G^0(\mathbf{k}, \omega)$ on a discretized k grid of 512 k points in each dimension, and fixed the energy broadening parameter $\Gamma = 1$ meV.

For the nearest-neighbor cubic model discussed here, we use an isotropic s-wave Gaussian Wannier function,

$$W(\mathbf{r}) = e^{-\mathbf{r}^2/2C^2\sigma^2}, \tag{6}$$

with $C = \sqrt{2 \ln 100}$ as the Wannier function. A Gaussian of this form ensures that the correct radial decay for the atomic wave functions at surfaces is captured, while allowing us to tune the overall radius of the Gaussian by using the parameter σ, where $W(\mathbf{r} = \sigma) = 0.01$. Here, we choose a value of $\sigma = 1.8$, in units of the lattice constant, to ensure sufficient overlap between nearest-neighbor atoms, while ensuring the next-nearest-neighbor overlap can be neglected. The choice of this parameter does not affect the qualitative behavior of the QPI vectors as we show in the Supplemental Material [25].

The cLDOS, Eq. (2), is then calculated on a large real-space grid over r_x and r_y at a fixed height $r_z = h$, and the 2D Fourier transform is taken to generate $\tilde{\rho}(\mathbf{q}_\parallel, \omega)$ which can be compared with experimental measurements.

To understand the influence of the 3D electronic structure on QPI measurements, we begin by considering the simple cubic lattice with nearest-neighbor hopping,

$$H(\mathbf{k}) = t_x \cos(k_x) + t_y \cos(k_y) + t_z \cos(k_z). \tag{7}$$

We then consider two scenarios, one where the defect is located deep in the bulk of the material, as sketched in Fig. 1(a), and the second for a defect located at the surface of a large slab, as sketched in Fig. 1(b). For the former we calculate Eq. (1) using the Hamiltonian in Eq. (7), whereas for the surface calculation we first perform a coordinate transformation

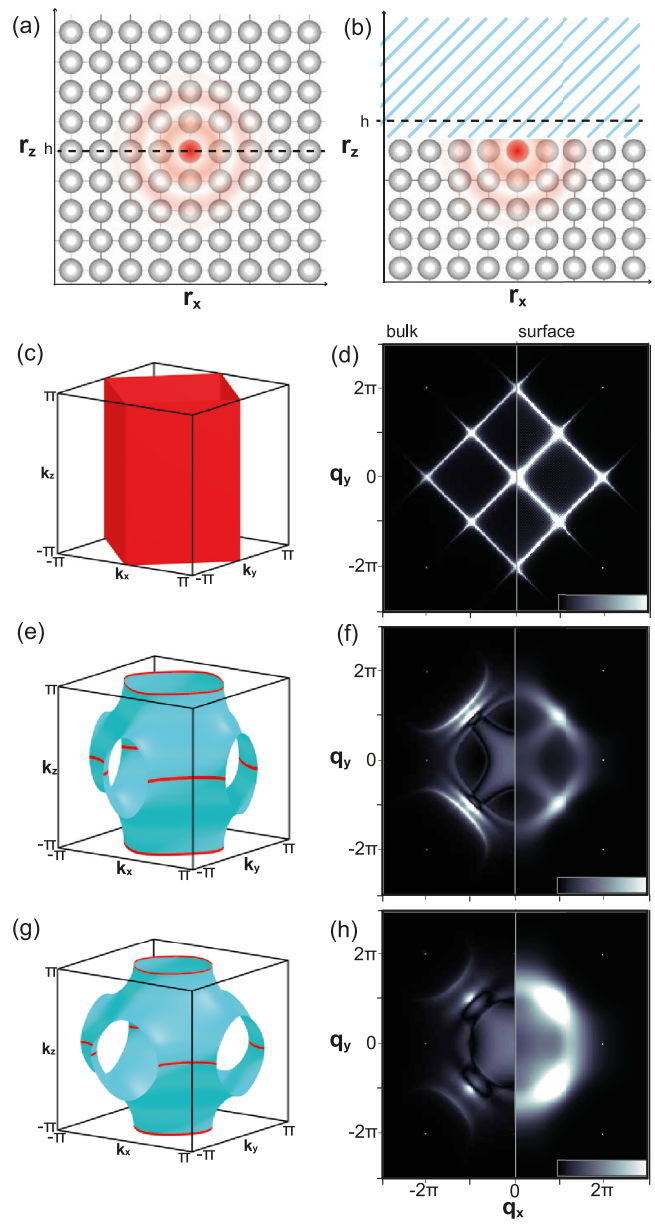

FIG. 1. Consequence of out-of-plane hopping on the bulk and surface QPI patterns. (a), (b) Sketch of the two scenarios considered: (a) a defect situated in the bulk of a material, and (b) a defect at the surface of a material. Here, h refers to the 2D plane used to study the Fourier transformation of the local density of states. (c), (d) 3D Fermi surface and cQPI $\tilde{\rho}(\mathbf{q}_\parallel, \omega)$ at $r_z = h$, calculated for the bulk defect (left half) and surface defect (right half) for the nearest-neighbor cubic model with $t_x = t_y = 0.1$ and $t_z = 0$. (e), (f) Equivalent simulations for $t_z = 0.05$, (g), (h) $t_z = 0.1$ (isotropic case). The surface projected spectral functions are plotted in Fig. S2 in the Supplemental Material [25].

to an N-layered slab,

$$H(\mathbf{k}_\parallel) = \begin{pmatrix} H^0(\mathbf{k}_\parallel) & H^1(\mathbf{k}_\parallel) & H^2(\mathbf{k}_\parallel) & \cdots \\ H^1(\mathbf{k}_\parallel) & H^0(\mathbf{k}_\parallel) & H^1(\mathbf{k}_\parallel) & \cdots \\ H^2(\mathbf{k}_\parallel) & H^1(\mathbf{k}_\parallel) & H^0(\mathbf{k}_\parallel) & \cdots \\ \cdots & \cdots & \cdots & \cdots \end{pmatrix}, \tag{8}$$

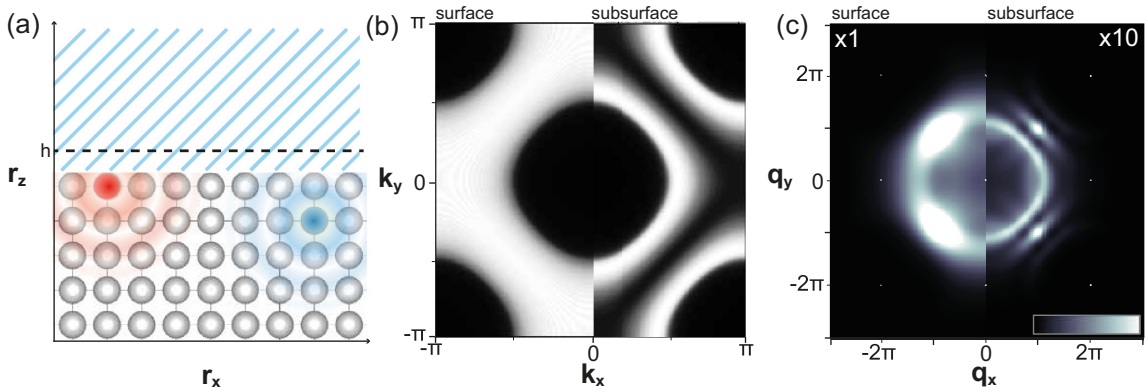

FIG. 2. Consequence of defect position for measured QPI. (a) Sketch of defects at different positions from the surface. (b) Partial spectral function of the surface layer (left half) and subsurface layer (right half). (c) cQPI $\tilde{\rho}(\mathbf{q}_\parallel, \omega)$ for a defect located at the surface [left half, red atom in (a)] and subsurface [right half, blue atom in (a)]. The intensity of the simulated cQPI due to a subsurface defect has been enhanced by a factor of 10 for comparison with the surface cQPI pattern.

where we have separated the Hamiltonian such that each row and column in the $N \times N$ block matrix describes a one-unit-cell thick layer along the z axis and the crystallographic momentum is now defined parallel to the x-y plane [$\mathbf{k}_\parallel = (k_x, k_y)$]. The individual elements are then defined as

$$H^{R_z}(\mathbf{k}_\parallel) = \sum_{\mathbf{R}_\parallel} H(\mathbf{R}_\parallel, R_z) e^{i\mathbf{k}_\parallel \mathbf{R}_\parallel}. \tag{9}$$

For the nearest-neighbor cubic model, $H(\pm 1, 0, 0) = t_x$, $H(0, \pm 1, 0) = t_y$, $H(0, 0, \pm 1) = t_z$.

Without loss of generality we assume that the surface does not distort the physical structure, nor induce any charge imbalance. To describe these would require modification of $H^0(\mathbf{k}_\parallel)$ for the surface layer(s) in Eq. (8).

III. RESULTS

We begin by comparing the QPI pattern in the cLDOS (cQPI) at the Fermi level expected from a bulk or surface calculation when out-of-plane hopping is neglected ($t_z = 0$). We find that the two-dimensional square Fermi surface [Fig. 1(c)] will produce a square QPI pattern, regardless of whether a bulk or surface defect is considered. This is shown in the left- and right-hand sides of Fig. 1(d), respectively. This is expected, as the slab Hamiltonian of Eq. (8) will be diagonal in the absence of out-of-plane hopping [$H^1(\mathbf{k}_\parallel) = 0$]. As t_z is increased, however, the differences between a bulk and surface cQPI simulation become increasingly apparent. Bulk simulations, shown on the left-hand side of Figs. 1(f) and 1(h), produce several sharp scattering vectors, which can be linked predominately to the nesting of states with $k_z = 0$ or $k_z = \pi$, shown as red lines in Figs. 1(e) and 1(g), as well as some broader intensity emanating from the center due to poorly nested scattering between the states with different k_z. Surface cQPI simulations do not produce such sharp scattering vectors. While the qualitative features do resemble those observed for bulk calculations, the uncertainty in k_z produces much broader scattering vectors and this broadness increases with increasing t_z.

As all experimental measurements are performed above the surface of a material, this implies that measurements on materials with a highly three-dimensional electronic structure will observe broad QPI scattering patterns from surface defects. Nevertheless, the presence of a surface also creates an additional consideration about the position of the defect. While in a bulk material, defects in different unit cells will only induce a phase shift in the simulated cQPI, near the surface, the depth of the defect generates unique environments [Fig. 2(a)]. This will alter the possible scattering vectors that can be observed. To illustrate this, we plot in Fig. 2(b) the partial spectral function $A^z(\mathbf{k}_\parallel, \omega)$ for the surface and subsurface layers of the nearest-neighbor cubic model with isotropic hopping,

$$A^z(\mathbf{k}_\parallel, \omega) = -\frac{1}{\pi} \mathrm{Im}\, G^{zz}(\mathbf{k}_\parallel, \omega), \tag{10}$$

with G^{zz} being the matrix element of the noninteracting Green's function for the zth layer of the N-layer slab [25]. Here, we observe that the electronic states at the surface have a very different spectral density depending on whether we are looking at the surface unit cell [left-hand side of Fig. 2(b)] or the subsurface unit cell [right-hand side of Fig. 2(b)]. At the surface, the spectral weight is spread out over the entire range of $\mathbf{k}_\parallel$ spanned by the bulk 3D Fermi surface [Fig. 1(g)] with a maximum intensity at $k_z = \frac{\pi}{2}$, whereas the subsurface spectral function exhibits a suppression of spectral weight around $k_z = \frac{\pi}{2}$ and maximum intensity around $k_z = \frac{\pi}{4}$ and $\frac{3\pi}{4}$. It is also found that the projected spectral function at deeper layers will introduce additional nodes which eventually converge to the bulk k_z averaged spectral function for a large number of layers N in the slab, as shown in Fig. S2 in the Supplemental Material [25].

This effect is a consequence of quantum interference in the z direction due to the surface breaking the translation symmetry resulting in resonatorlike states in the vicinity of the surface, much as the quasiparticle interference of a one-dimensional defect in a 2D electron gas [1]. This has a pronounced effect on the spectral function, modulating the spectral density of the states in different depths and thus the strength with which scattering vectors for defects located at certain depths are observed. QPI scattering vectors arising from subsurface and deeper defects will produce qualitatively different patterns compared to surface defects, as shown in Fig. 2(c), and these scattering vectors can be related to the

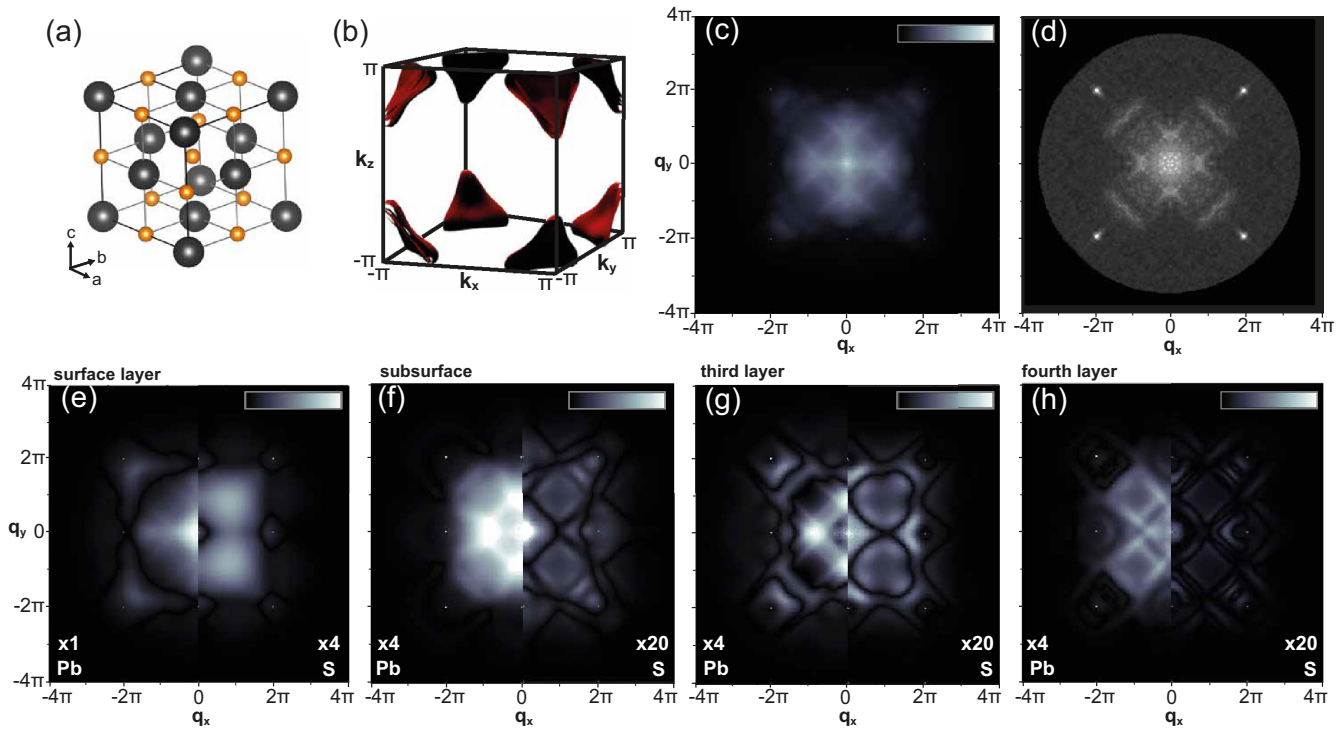

FIG. 3. cQPI calculation for the rocksalt structure PbS. (a) Crystal structure of PbS, with larger black atoms as Pb and smaller orange atoms as S. (b) 3D electronic structure taken at $E = 1$ eV above the Fermi level. (c) Total QPI pattern obtained via calculating Eq. (11) of the main text with the weights α_i set to 1. The sum was performed over four Pb defects from the top four surface layers and four S defects from the top four surface layers. (d) Experimental differential conductance QPI image of PbS from Ref. [22], taken at $V = 0.80$ eV. The individual contributions to (c) are shown in (e)–(h). The scattering patterns originating from Pb-site defects at a specific depth are shown on the left-hand side of each panel and the ones originating from S defects are shown on the right-hand side. The maximum intensity of the color scale has been defined relative to the left-hand side of (e).

full three-dimensional electronic structure of the bulk material by analyzing the corresponding spectral function at a specific depth from the surface. For defects at a known depth, one may use this knowledge to extract information about the k_z dispersion of the full three-dimensional electronic structure, or, conversely, for a known electronic structure the scattering pattern can be used to determine the defect depth. We note that this is a general phenomenon resulting in a modulation of the spectral function $A^z(k_\parallel, \omega)$ as a function of depth z.

It is worth noting that the intensity of the QPI from subsurface defects is rather weak. As illustrated in Fig. 2(c), the intensity of QPI arising from a subsurface defect in this toy model is only 10% of that from a surface defect. Nevertheless, this does not imply that the QPI from these defects cannot be observed. In fact, it implies that if one wishes to directly reproduce experimental measurements of QPI arising from 3D systems, then one needs to sum the contribution of all types of defects, i, not just of different elements, but from different sites and depths, to the total cLDOS $[\rho^i(\mathbf{q}, \omega)]$, and multiply these by a realistic approximation for the different number of each type of defect,

$$\rho^{\text{expt}}(\mathbf{q}_\parallel, \omega) = \sum_i \alpha_i \rho^i(\mathbf{q}_\parallel, \omega). \tag{11}$$

In some systems, it may be sufficient to only consider surface defects, however, this will be dependent on the materials' chemical composition and the relative number of each type of defect. For intrinsic bulk defects, α_i should be approximately equal and independent of i.

To illustrate this, in Fig. 3 we present equivalent cQPI slab calculations for a density functional theory (DFT)-derived tight-binding model of PbS, a semiconducting rocksalt material shown in Fig. 3(a) where QPI measurements have recently been reported [22]. The valence bands of this material are dominated by the p orbitals of Pb and at an energy of 1 eV above the Fermi level exhibits a 3D electronic structure with no states around $k_z = 0$, as shown in Fig. 3(b). This model was generated using QUANTUM ESPRESSO [26] and WANNIER90 [27], and details can be found in the Supplemental Material [25]. In Fig. 3(c), we present the result of calculating Eq. (11) for a 16-unit-cell-thick slab of PbS, for the (100) surface, assuming all Pb and S defects are equally likely. This produces a complex pattern which is in good qualitative agreement with the experimental QPI measurement from Ref. [22] at a similar energy (0.8 eV) shown in Fig. 3(d).

Figures 3(e)–3(h) reveal the power of the methodology employed here. Each Pb defect (left) and S defect (right) that was considered produces a unique QPI scattering pattern depending on the relative distance from the surface, and it can be seen that some scattering patterns [e.g., left-hand side in Figs. 3(f) and 3(h)] are remarkably similar to the experimental measurement. This could suggest an uneven distribution of α_i in this system [22] and highlights that this numerical simulation technique can be used to identify not only the

three-dimensional electronic structure of a system but also the relative concentration of unique defects at or below the surface, assuming the electronic structure is sufficiently well understood. To confirm if this defect anisotropy is generic, one could perform DFT-based slab calculations and study the energy of each type of defect. However, this is beyond the scope of the present work.

IV. DISCUSSION

Our analysis of cQPI simulations for three-dimensional systems highlights an important consideration regarding the comparison and interpretation of QPI measurements. Defects of the same type, but at different distances from the surface, will produce unique sets of scattering vectors governed by unique regions of k_z. It implies that if one wishes to truly compare and understand the electronic structure of 3D materials using QPI, one needs to compare the experimental measurement with a simulation that takes into account multiple defects not just of different types, but at different depths from the surface. Additionally, unless surface states are present [28–30], if the system exhibits non-negligible out-of-plane hopping, the sharpest QPI features present in Fourier-transformed measurements will originate not from defects at the surface but from subsurface defects. In cases where a surface state exist, e.g., on the noble metal (111) surface [31] the surface state scattering will dominate the scattering intensity.

These details were not captured in previous theoretical studies of three-dimensional systems [18,22,28,32], due to the use of discrete, site-centered Green's functions. The continuum transformation employed here is therefore a very useful tool to reliably and accurately compare STM measurements with theoretical simulations for generic materials.

In this paper, we performed the continuum transformation assuming Gaussian- or Slater-type orbitals, and left the radii of these orbitals as a free parameter which could be fit to experimental measurements [25], however, it is also possible to more accurately capture the orbital overlap and decay into vacuum by explicitly calculating the Wannier orbitals, e.g., from density functional theory [10,23,24]. This may be required in more complex systems with multiple atomic elements, particularly in systems where the surface layer does not contribute any states to the Fermi level.

To summarize, we have studied how out-of-plane hopping modifies the electronic response in realistic simulations of QPI. Our results provide a generic framework to understand this behavior, and highlight the importance of defect depth, position, and type on experimental observables. The methods introduced here unlock the ability to understand the three-dimensional electronic structure of materials using scanning tunneling microscopy. The formalism presented here can be used analogously to describe the behavior of magnons [33] or phonons near surfaces, providing a broader framework to describe how quasiparticles can be detected at the surfaces.

Underpinning data are available at Ref. [34].

ACKNOWLEDGMENTS

L.C.R. acknowledges support through the Royal Commission for the Exhibition 1851 and C.A.M. and P.W. from the Engineering and Physical Sciences Research Council (EPSRC EP/L015110/1, EP/S005005/1, and EP/R031924/1).

[1] M. F. Crommie, C. P. Lutz, and D. M. Eigler, Imaging standing waves in a two-dimensional electron gas, Nature (London) **363**, 524 (1993).

[2] Y. Hasegawa and Ph. Avouris, Direct Observation of Standing Wave Formation at Surface Steps using Scanning Tunneling Spectroscopy, Phys. Rev. Lett. **71**, 1071 (1993).

[3] C. R. Ast, B. Jäck, J. Senkpiel, M. Eltschka, M. Etzkorn, J. Ankerhold, and K. Kern, Sensing the quantum limit in scanning tunnelling spectroscopy, Nat. Commun. **7**, 13009 (2016).

[4] L. Petersen, P. T. Sprunger, Ph. Hofmann, E. Lægsgaard, B. G. Briner, M. Doering, H.-P. Rust, A. M. Bradshaw, F. Besenbacher, and E. W. Plummer, Direct imaging of the two-dimensional Fermi contour: Fourier-transform STM, Phys. Rev. B **57**, R6858 (1998).

[5] L. Simon, C. Bena, F. Vonau, M. Cranney, and D. Aubel, Fourier-transform scanning tunnelling spectroscopy: The possibility to obtain constant-energy maps and band dispersion using a local measurement, J. Phys. D: Appl. Phys. **44**, 464010 (2011).

[6] J. E. Hoffman, Imaging quasiparticle interference in $Bi_2Sr_2CaCu_2O_{8+\delta}$, Science **297**, 1148 (2002).

[7] Y. Kohsaka, C. Taylor, P. Wahl, A. Schmidt, J. Lee, K. Fujita, J. W. Alldredge, K. McElroy, J. Lee, H. Eisaki, S. Uchida, D.-H. Lee, and J. C. Davis, How Cooper pairs vanish approaching the Mott insulator in $Bi_2Sr_2CaCu_2O_{8+\delta}$, Nature (London) **454**, 1072 (2008).

[8] Y. He, Y. Yin, M. Zech, A. Soumyanarayanan, M. M. Yee, T. Williams, M. C. Boyer, K. Chatterjee, W. D. Wise, I. Zeljkovic, T. Kondo, T. Takeuchi, H. Ikuta, P. Mistark, R. S. Markiewicz, A. Bansil, S. Sachdev, E. W. Hudson, and J. E. Hoffman, Fermi surface and pseudogap evolution in a cuprate superconductor, Science **344**, 608 (2014).

[9] Z. Wang, D. Walkup, P. Derry, T. Scaffidi, M. Rak, S. Vig, A. Kogar, I. Zeljkovic, A. Husain, L. H. Santos, Y. Wang, A. Damascelli, Y. Maeno, P. Abbamonte, E. Fradkin, and V. Madhavan, Quasiparticle interference and strong electron–mode coupling in the quasi-one-dimensional bands of Sr_2RuO_4, Nat. Phys. **13**, 799 (2017).

[10] A. Kreisel, C. A. Marques, L. C. Rhodes, X. Kong, T. Berlijn, R. Fittipaldi, V. Granata, A. Vecchione, P. Wahl, and P. J. Hirschfeld, Quasi-particle interference of the van Hove singularity in Sr_2RuO_4, npj Quantum Mater. **6**, 100 (2021).

[11] M. P. Allan, A. W. Rost, A. P. Mackenzie, Y. Xie, J. C. Davis, K. Kihou, C. H. Lee, A. Iyo, H. Eisaki, and T.-M. Chuang, Anisotropic energy gaps of iron-b superconductivity from intraband quasiparticle interference in LiFeAs, Science **336**, 563 (2012).

[12] M. P. Allan, K. Lee, A. W. Rost, M. H. Fischer, F. Massee, K. Kihou, C.-H. Lee, A. Iyo, H. Eisaki, T.-M. Chuang, J. C. Davis, and E.-A. Kim, Identifying the "fingerprint" of antiferromagnetic spin fluctuations in iron pnictide superconductors, Nat. Phys. **11**, 177 (2015).

[13] P. O. Sprau, A. Kostin, A. Kreisel, A. E. Böhmer, V. Taufour, P. C. Canfield, S. Mukherjee, P. J. Hirschfeld, B. M. Andersen, and J. C. S. Davis, Discovery of orbital-selective Cooper pairing in FeSe, Science **357**, 75 (2017).

[14] A. R. Schmidt, M. H. Hamidian, P. Wahl, F. Meier, A. V. Balatsky, J. D. Garrett, T. J. Williams, G. M. Luke, and J. C. Davis, Imaging the Fano lattice to "hidden order" transition in URu_2Si_2, Nature (London) **465**, 570 (2010).

[15] B. B. Zhou, S. Misra, E. H. da Silva Neto, P. Aynajian, R. E. Baumbach, J. D. Thompson, E. D. Bauer, and A. Yazdani, Visualizing nodal heavy fermion superconductivity in $CeCoIn_5$, Nat. Phys. **9**, 474 (2013).

[16] A. Akbari, P. Thalmeier, and I. Eremin, Quasiparticle interference in the heavy-fermion superconductor $CeCoIn_5$, Phys. Rev. B **84**, 134505 (2011).

[17] T. Hanaguri, K. Iwaya, Y. Kohsaka, T. Machida, T. Watashige, S. Kasahara, T. Shibauchi, and Y. Matsuda, Two distinct superconducting pairing states divided by the nematic end point in $FeSe_{1-x}S_x$, Sci. Adv. **4**, eaar6419 (2018).

[18] L. C. Rhodes, M. D. Watson, T. K. Kim, and M. Eschrig, k_z Selective Scattering within Quasiparticle Interference Measurements of FeSe, Phys. Rev. Lett. **123**, 216404 (2019).

[19] A. Weismann, M. Wenderoth, S. Lounis, P. Zahn, N. Quaas, R. G. Ulbrich, P. H. Dederichs, and S. Blügel, Seeing the Fermi surface in real space by nanoscale electron focusing, Science **323**, 1190 (2009).

[20] S. Lounis, P. Zahn, A. Weismann, M. Wenderoth, R. G. Ulbrich, I. Mertig, P. H. Dederichs, and S. Blügel, Theory of real space imaging of Fermi surface parts, Phys. Rev. B **83**, 035427 (2011).

[21] T. Kotzott, M. Bouhassoune, H. Prüser, A. Weismann, S. Lounis, and M. Wenderoth, Scanning tunneling spectroscopy of subsurface Ag and Ge impurities in copper, New J. Phys. **23**, 113044 (2021).

[22] C. A. Marques, M. S. Bahramy, C. Trainer, I. Marković, M. D. Watson, F. Mazzola, A. Rajan, T. D. Raub, P. D. C. King, and P. Wahl, Tomographic mapping of the hidden dimension in quasiparticle interference, Nat. Commun. **12**, 6739 (2021).

[23] P. Choubey, T. Berlijn, A. Kreisel, C. Cao, and P. J. Hirschfeld, Visualization of atomic-scale phenomena in superconductors: Application to FeSe, Phys. Rev. B **90**, 134520 (2014).

[24] A. Kreisel, P. Choubey, T. Berlijn, W. Ku, B. M. Andersen, and P. J. Hirschfeld, Interpretation of Scanning Tunneling Quasiparticle Interference and Impurity States in Cuprates, Phys. Rev. Lett. **114**, 217002 (2015).

[25] See Supplemental Material at http://link.aps.org/supplemental/10.1103/PhysRevB.107.045107 for details regarding the choice of Wannier function radius, the full evolution of the partial spectral function as a function of z, as well as details of the generation of the PbS tight binding model.

[26] P. Giannozzi, O. Andreussi, T. Brumme, O. Bunau, M. B. Nardelli, M. Calandra, R. Car, C. Cavazzoni, D. Ceresoli, M. Cococcioni, N. Colonna, I. Carnimeo, A. D. Corso, S. de Gironcoli, P. Delugas, R. A. DiStasio, Jr., A. Ferretti, A. Floris, G. Fratesi, G. Fugallo *et al.*, Advanced capabilities for materials modelling with Quantum ESPRESSO, J. Phys.: Condens. Matter **29**, 465901 (2017).

[27] G. Pizzi, V. Vitale, R. Arita, S. Blügel, F. Freimuth, G. Géranton, M. Gibertini, D. Gresch, C. Johnson, T. Koretsune, J. Ibañez-Azpiroz, H. Lee, J.-M. Lihm, D. Marchand, A. Marrazzo, Y. Mokrousov, J. I. Mustafa, Y. Nohara, Y. Nomura, L. Paulatto *et al.*, Wannier90 as a community code: New features and applications, J. Phys.: Condens. Matter **32**, 165902 (2020).

[28] F. Lambert, A. Akbari, P. Thalmeier, and I. Eremin, Surface State Tunneling Signatures in the Two-Component Superconductor UPt_3, Phys. Rev. Lett. **118**, 087004 (2017).

[29] S. Pinon, V. Kaladzhyan, and C. Bena, Surface Green's functions and boundary modes using impurities: Weyl semimetals and topological insulators, Phys. Rev. B **101**, 115405 (2020).

[30] P. Rüßmann, P. Mavropoulos, and S. Blügel, *Ab initio* theory of Fourier-transformed quasiparticle interference maps and application to the topological insulator Bi_2Te_3, Phys. Status Solidi B **258**, 2000031 (2021).

[31] L. Petersen, P. Laitenberger, E. Lægsgaard, and F. Besenbacher, Screening waves from steps and defects on Cu(111) and Au(111) imaged with STM: Contribution from bulk electrons, Phys. Rev. B **58**, 7361 (1998).

[32] P. G. Derry, A. K. Mitchell, and D. E. Logan, Quasiparticle interference from magnetic impurities, Phys. Rev. B **92**, 035126 (2015).

[33] A. Mitra, A. Corticelli, P. Ribeiro, and P. A. McClarty, Magnon interference tunneling spectroscopy as a probe of 2D magnetism, arXiv:2110.02662.

[34] L. C. Rhodes, W. Osmolska, C. A. Marques, and P. Wahl, Data set for "Nature of quasiparticle interference in three dimensions", University of St Andrews Research Portal, https://doi.org/10.17630/723d7ab4-1ee6-40ec-899c-4e5ce0a67060 (2022).